ELSEVIER

Journal of Fluids and Structures 23 (2007) 1168–1188

JOURNAL OF FLUIDS AND STRUCTURES

www.elsevier.com/locate/jfs

# A numerical investigation of the effects of the spanwise length on the 3-D wake of a circular cylinder

D.F.L. Labbé[1], P.A. Wilson*

*School of Engineering Sciences, University of Southampton, SO17 1BJ, UK*

Received 21 January 2005; accepted 3 May 2007
Available online 6 August 2007

**Abstract**

The numerical prediction of vortex-induced vibrations has been the focus of numerous investigations to date using tools such as computational fluid dynamics. In particular, the flow around a circular cylinder has raised much attention as it is present in critical engineering problems such as marine cables or risers. Limitations due to the computational cost imposed by the solution of a large number of equations have resulted in the study of mostly 2-D flows with only a few exceptions. The discrepancies found between experimental data and 2-D numerical simulations suggested that 3-D instabilities occurred in the wake of the cylinder that affect substantially the characteristics of the flow. The few 3-D numerical solutions available in the literature confirmed such a hypothesis. In the present investigation the effect of the spanwise extension of the solution domain on the 3-D wake of a circular cylinder is investigated for various Reynolds numbers between 40 and 1000. By assessing the minimum spanwise extension required to predict accurately the flow around a circular cylinder, the infinitely long cylinder is reduced to a finite length cylinder, thus making numerical solution an effective way of investigating flows around circular cylinders. Results are presented for three different spanwise extensions, namely $\pi D/2$, $\pi D$ and $2\pi D$. The analysis of the force coefficients obtained for the various Reynolds numbers together with a visualization of the three-dimensionalities in the wake of the cylinder allowed for a comparison between the effects of the three spanwise extensions. Furthermore, by showing the different modes of vortex shedding present in the wake and by analysing the streamwise components of the vorticity, it was possible to estimate the spanwise wavelengths at the various Reynolds numbers and to demonstrate that a finite spanwise extension is sufficient to accurately predict the flow past an infinitely long circular cylinder.
© 2007 Elsevier Ltd. All rights reserved.

*Keywords:* Circular cylinder; Three-dimensional wake; Numerical; Simulation

## 1. Introduction

Vortex-induced vibration (VIV), or flow-induced vibration (FIV), as it is sometimes referred to, has been the subject of intensive research for many years as it is present in numerous practical applications such as in offshore engineering. As the oil-field development activities moved into deeper waters and areas of stronger ocean currents, the importance of (VIVs) becomes critical at the system design stages (Cook et al., 2000) as it can result in serious fatigue failure or

*Corresponding author.
*E-mail address:* philip.wilson@soton.ac.uk (P.A. Wilson).
[1]Present address: Houlder Offshore Engineering Limited, 59 Lafone Street, London, UK.

0889-9746/$ - see front matter © 2007 Elsevier Ltd. All rights reserved.
doi:10.1016/j.jfluidstructs.2007.05.005

interference and clashing. As most of the interesting fluid dynamic phenomena are present (Dalton, 2000) such as boundary layer and boundary layer separation, laminar and turbulent flow, shear layer and shear layer roll up, vortices and vortex shedding, and unsteady lift and drag, the task of capturing or predicting all of these represents a major challenge.

The study of the flow around circular cylinders has been the centre of many investigations over the last 100 years and it is now common knowledge that the flow around cylinders can be characterized essentially by two parameters, namely the Reynolds number $\mathrm{Re} = UD/\nu$ and the Strouhal number $\mathrm{St} = fD/U$, where $U$ the upstream velocity, $D$ is the cylinder diameter, $\nu$ the kinematic viscosity of the flow and $f$ the frequency of the shedding of vortices from the cylinder.

The first definition of the flow regimes around a circular cylinder was given by Roshko (1955) who established a Strouhal–Reynolds number relationship. His measurements of the velocity fluctuations, spectra and frequency allowed for the identification of a transitional region for $150 \leqslant \mathrm{Re} \leqslant 300$, while distinct irregularities could be observed for $\mathrm{Re} > 300$.

Further evidence was provided in Williamson (1988) of the transition from 2-D to 3-D flows in the Strouhal–Reynolds number relationship. Williamson also identified two stages in the transition to 3-D flows, characterized by two discontinuities in the Strouhal–Reynolds number relationship, the first one at $\mathrm{Re} = 178$ and the second for $230 \leqslant \mathrm{Re} \leqslant 260$. Williamson further associated those discontinuities with a mode change in the shedding of vortices in the cylinder wake (Williamson, 1996). The first mode, named mode A is characterized by the inception of streamwise vortex loops. The primary vortices roll up and deform in a wavy pattern along their length during the process of shedding to result in the local spanwise formation of vortex loops. The second mode, namely mode B, associated with the second discontinuity, is characterized by the formation of finer-scale streamwise vortex pairs.

Reviewing the numerical simulations of vortex shedding, Williamson also noted the very good agreement found between 3-D direct numerical simulation and experimental results and how the numerical solutions were capable of capturing the two mode changes (Thompson et al., 1996). He further commented that the discontinuities observed in the Strouhal–Reynolds number relationship were not achieved with 2-D numerical solutions as can be seen in Fig. 1.

In their study of 3-D vortex structures in a cylinder wake, Wu et al. (1996) used digital particle imaging velocimetry (DPIV) to measure the instantaneous velocity field in the vertical plane in the near wake of a cylinder at $\mathrm{Re} = 525$. The measured velocity field was then used to compute accurately the vorticity field. No visual evidence of the presence of the two transitional modes presented by Williamson were found, but the importance of vortex stretching was shown. An interesting comment raised by Wu et al. (1996) in the observation of the results is the remarkable regularity of the vortices in the streamwise and spanwise directions, although some variability appeared due to the distortion of the vortex sheet.

Numerical simulations of VIV excitation of circular cylinders using the solution of the Navier–Stokes equations have been the focus of numerous studies in the literature, but essentially restricted to the 2-D simulations owing to the limitation of the computational resources. Several aspects of the fluid-structure interactions are examined in these works, among which are the computation of the forces acting on the cylinder, the shedding of vortices from the cylinder, and the wake of the cylinder. But as the Reynolds numbers of interest for practical flow problems can range from $10^5$ to $10^6$ (Vandiver, 2000), researchers focussed their numerical investigations on higher Reynolds numbers and started encountering discrepancies between their 2-D numerical results and the experimental data.

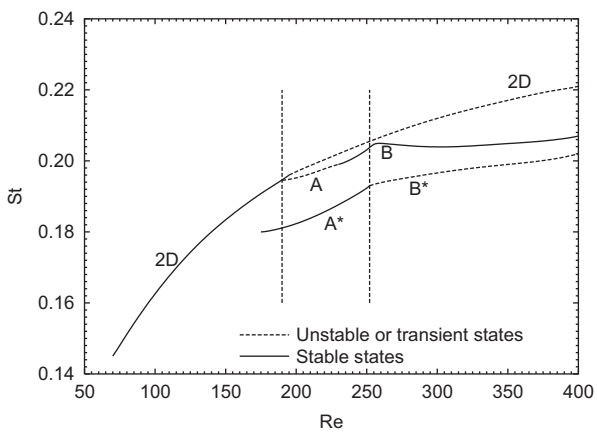


Fig. 1. Strouhal–Reynolds number relationship [from (Williamson, 1996)].

The 3-D flow around a circular cylinder in a uniform flow was studied in Kalro and Tezduyar (1997) and found that the results obtained for the Re = 300 compared well with the 2-D results. Since 3-D effects appear for Re ≈ 190, this indicates that, for Re = 300, weak 3-D features are present. On the other hand, the results they obtained for Re = 800 were clearly different from the 2-D ones, indicating that the 3-D features were much stronger. They concluded that, as the boundary layer is thinner at higher Reynolds number, the velocity gradients in the near-cylinder region are much larger, thus implying the release of stronger vortices. It follows that the amplitude of the force coefficients in 2-D simulations is larger at Re = 800 than at Re = 300. However, this is not seen in the 3-D computations since the vortices are significantly distorted and possess components in addition to those in the spanwise directions.

The flow around 3-D cylinders at Re = 100 and 200 was studied by Zhang and Dalton (1998), confirming the 2-D nature of the flow for the Re = 100 case. However, their results for the Re = 200 case clearly show the presence of distinct 3-D features and emphasized that the flow in the wake was becoming 3-D before it even becomes turbulent. Furthermore, their studies stressed the importance of the proper representation of the flow in the wake as it has a noticeable effect on the force coefficients and the Strouhal number. Zhang and Dalton also commented that, as 2-D computations were still cheaper than 3-D solutions, if a cautious estimate of the effect of the lack of 3-D features could be established, 2-D simulations could still provide a qualitative understanding of the flow.

Further details are presented in Breuer (1998) of the differences between the 2-D and 3-D computations by showing, at Re = 3900, the striking differences in the time-averaged streamline patterns characterized by the absence, in 2-D results, of a recirculation zone behind the cylinder clearly showing in the 3-D results. Breuer noted that the 2-D field was more asymmetrical than the 3-D one as the vortices shed from the cylinder moved downstream along an axis which is inclined with reference to the symmetry line. As a consequence, the drag coefficient and the base pressure coefficient were much too high in 2-D computations. He thus concluded that, even for nearly 2-D flow problems, 2-D computations were useless as 3-D structures strongly influenced the near-wake flow.

In a later publication on the influence of subgrid-scale models for large-eddy simulations around circular cylinders in 3-D, Breuer (2000) noted that the flow around the circular cylinder was not only a function of the Reynolds number, but also, among other factors, it was a function of the cylinder aspect ratio. He thus stressed that the difference between numerical and experimental results were apparent and that the most relevant factor to evaluate numerical simulations was the spanwise extension of the integration domain, often limited due to computational resources.

It is thus clear that 2-D numerical solutions are inadequate to describe practical flow problems, as they result in an erroneous representation of the wake of the cylinder and cannot reproduce the 3-D features occurring above Re ≈ 190. Also, it has been found that 3-D simulations were in good agreement with experimental results. However, such simulations are highly dependent on the spanwise extension of the domain considered. Furthermore, to accurately predict the flow past the circular cylinder, particular attention has to be paid to the representation of the flow field in the near vicinity of the cylinder and in its wake. An interesting issue concerns the aspect of the wake of the cylinder at low Reynolds number. As it has been reported (Williamson, 1988) that the vortex pattern was remarkably regular in the spanwise directions, and moreover that a spanwise periodicity of the flow occurs in the wake, one can wonder, if such a periodicity exists, what is its spanwise extension and how it is affected by the different flow regimes? If a periodicity really occurs in the spanwise direction, the problem of an infinitely long cylinder in a flow would be reduced to that of a flow past a finite length cylinder, therefore reducing the computational cost substantially.

In their study of the effect of the spanwise length on the modelling of flow over a circular cylinder, Lei et al. (2001) concluded that a spanwise length less than two cylinder diameters was insufficient to achieve reliable results. Furthermore, the quasiperiodic beat phenomenon observed experimentally in the lift and drag coefficient history can only be observed for 3-D simulations with a spanwise extension greater than twice the cylinder diameter. However, their investigation was carried out for Re = 1000.

Furthermore, in the same study, the results obtained with a spanwise extension of four cylinder diameters suggested there might be a relationship between this particular spanwise length and the real spanwise wavelength at Re = 1000. Since all the numerical solutions encountered in the literature are carried out with periodic boundary conditions on the upper and lower part of the domain, a pseudo-periodicity is forced onto the flow. This implies that a reliable solution using the periodic boundary condition can only be achieved if the extension matches an exact number of spanwise wavelengths. It is however difficult, at the present stage of the research for flow around a circular cylinder, to predict accurately such a spanwise wavelength.

The aim of the present research is to investigate the wake behind a circular cylinder and determine the influence of the spanwise extension of the solution domain onto the 3-D solution for $100 \leqslant \mathrm{Re} \leqslant 1000$. By carrying the solution to different spanwise extensions and visualizing the 3-D features in the wake of the cylinder, the influence of the spanwise extension of the domain on the solution will be assessed. It will then be possible to determine the minimum spanwise extension required to capture accurately the 3-D flows around the cylinder.

## 2. Numerical method

To carry out the numerical investigation of the effects of the spanwise extension on the flow past a circular cylinder, a parallel 3-D incompressible Navier–Stokes equations solver on block-structured grids was developed. The complete method, its implementation and validation can be found in Labbé (2004).

A numerical solution is composed of several components. The first and most critical one is the mathematical formulation of the problem. For the purpose of the present work, the incompressible Navier–Stokes equations expressed in body-fitted coordinates (i.e., curvilinear coordinates) and filtered for the large eddy simulation turbulence model are the most suitable. In a nondimensional form and using the tensor notation the flow governing equations can be written as follows:

*Continuity*:

$$\frac{\partial(J\overline{U^i})}{\partial\xi_i} = 0; \tag{1}$$

*Momentum*:

$$\frac{\partial}{\partial t}(J\bar{u}_i^*) + \frac{\partial}{\partial\xi_k}(\overline{U_r}^{*k}\bar{u}_i^*) = -J^{-1}S_i^j\frac{\partial\bar{q}}{\partial\xi_j} + \frac{\partial}{\partial\xi_k}\left[\left(\frac{1}{\mathrm{Re}} + \frac{1}{\mathrm{Re}_t}\right)\left(J^{-1}S_j^kS_j^l\frac{\partial\bar{u}_i^*}{\partial\xi_l}\right)\right]; \tag{2}$$

where $\mathrm{Re}_t$ is the turbulent Reynolds number as obtained using one of the Structure Function LES models in Métais and Lesieur (1992),

$$\mathrm{Re}_t = \frac{U_\infty D}{0.063\Delta\sqrt{\bar{F}_2(\xi,\Delta t)}}, \tag{3}$$

with

$$\bar{F}_2 = \langle\|\mathbf{u}(\xi+\mathbf{r}) - \mathbf{u}(\xi)\|^2\rangle_{\|\mathbf{r}\|=1}, \tag{4}$$

$\Delta$ is the filter width, usually taken as an average of the mesh sizes. Details of the flow-governing equations are presented in the Appendix A.1.

To solve the incompressible Navier–Stokes equations, the projection method as formulated originally by Chorin (1968) was chosen for its simplicity and efficiency. The projection method consists of three steps:

(i) The momentum equations are solved omitting the pressure terms, to obtain an intermediate velocity field that does not satisfy the continuity constraint.
(ii) The pressure is then solved by using the Poisson equation.
(iii) By using the pressure gradient, a provisional velocity field is projected onto a divergence-free space thus resulting in a velocity field complying with the continuity constraint.

To achieve these three steps, the equations governing the flow are discretized using the finite volume method on a collocated grid. The detailed description of the discretization and solution using parallel computation is presented in the Appendix.

## 3. Three-dimensional flow around a fixed circular cylinder

### 3.1. Numerical solution set-up

Preliminary 2-D studies were carried out by Labbé (2004) using several grid resolutions: $64 \times 64$, $128 \times 128$ and $256 \times 256$ and various LES models (Smagorinsky, structure function and selective structure function). The grid was an O-shaped grid with uniformly distributed cells around the perimeter of the cylinder and with the boundaries situated 15 cylinder diameters away from the cylinder.

When comparing the relationship between $C_{D_{\max}}$, $C_{L_{\max}}$ and Re, the influence of the turbulence model used for the solution can only be noted for $\mathrm{Re} \geqslant 250$. This can be expected, as little or no small scale instabilities are present in the flow for Reynolds number up to about 300.

In the case where no turbulence models were used, or when the Smagorinsky or selective structure function were used, both the lift and drag coefficients were overpredicted. Furthermore, the difference between the lift coefficient found numerically and the results found in the literature increased with the Reynolds number.

The Structure Function LES model whether applied using the $128 \times 128$ or $256 \times 256$ grid appeared to slightly underpredict the drag coefficient for Reynolds number up to about 800. However, this model produces very good results for the lift coefficients. Also, very small differences between the results on the two grids for this turbulence model could be noted (Table 1). Such a finding can be corroborated by those of Breuer (2000) who came to the conclusion that, when using LES models, greater refinement did not automatically lead to improvements in the results. The Structure Function LES turbulence model led to a prediction of the force coefficients in better agreement with the data from Williamson (1996) than other models, particularly for the $128 \times 128$ grid at high Reynolds numbers. As such, and taking into consideration the computational cost of a 3-D solution, the $128 \times 128$ grid will be used as a base for the 3-D solutions.

It is reported (Williamson, 1996) that there exist two distinct spanwise wavelengths depending on the vortex shedding modes. When mode A occurs, the wavelength is about four cylinder diameters, while at mode B, it varies around one cylinder diameter. Clearly, mode A requires a substantially greater spanwise extent of the domain than mode B and, if one is to capture it, the solution domain must extend at least four cylinder diameters in the spanwise direction.

In the context of the present investigation, three extensions were chosen, namely $\pi D/2$, $\pi D$ and $2\pi D$. This allows for the cells close to the cylinder surface to have an aspect ratio of 1. Table 2 gives the details of the three grids used here and Figs. 2 and 3 illustrate the solution domain in the case of Grid F. Grid E is composed of four blocks distributed across the perimeter of the cylinder as in the 2-D case, while grid F was composed of eight blocks, i.e., two layers of the grid blocks used in the grid E. Grid D was tested at a later stage and is composed of eight blocks, in the same configuration as for grid F, but each block a quarter the size of those of grid E. The reason for the greater number of blocks in comparison to the grid size for grid D was due to a time constraint and the need to carry out the solution at a faster pace. A symmetric boundary condition was applied for both upper and lower boundaries and a zero-gradient outflow on the aft part of the cylindrical domain lateral boundaries.

The solution obtained for the steady flow at $\mathrm{Re} = 40$ is used as an initial solution for all the other cases, increasing the Reynolds number progressively until reaching the desired value. The initial solution being converged, very few subiterations are required to resolve the pressure field at each time step, thus reducing the overall computation time.

A total of 60 simulations were carried out using the Iridis cluster of the University of Southampton. The processing nodes used were dual 1.8 GHz Xeon processors nodes with 2 GB of RAM interconnected by a myrinet network. Each node carried out the solution of two blocks of the mesh. Thus, the solutions on grid E required two nodes (total of four processors for four grid blocks) while the solution on grids F and D required four nodes (eight processors for eight grid blocks).

Table 1
Force coefficients for the 2-D simulations using the Structure Function LES model

| Re | St | $C_D$ | $C_v$ | $C_p$ | $C_L$ | Grid |
|---|---|---|---|---|---|---|
| 100 | 0.164 | 1.321 | 0.301 | 1.020 | 0.322 | $128 \times 128$ |
| 100 | 0.166 | 1.332 | 0.326 | 1.006 | 0.330 | $256 \times 256$ |
| 200 | 0.195 | 1.310 | 0.197 | 1.113 | 0.662 | $128 \times 128$ |
| 200 | 0.200 | 1.329 | 0.229 | 1.100 | 0.679 | $256 \times 256$ |
| 300 | 0.205 | 1.337 | 0.148 | 1.190 | 0.878 | $128 \times 128$ |
| 300 | 0.210 | 1.357 | 0.182 | 1.174 | 0.908 | $256 \times 256$ |
| 325 | 0.215 | 1.341 | 0.139 | 1.202 | 0.918 | $128 \times 128$ |
| 325 | 0.215 | 1.362 | 0.174 | 1.188 | 0.950 | $256 \times 256$ |
| 400 | 0.221 | 1.377 | 0.120 | 1.257 | 1.017 | $128 \times 128$ |
| 400 | 0.215 | 1.339 | 0.149 | 1.190 | 1.051 | $256 \times 256$ |
| 500 | 0.225 | 1.410 | 0.100 | 1.310 | 1.113 | $128 \times 128$ |
| 500 | 0.234 | 1.354 | 0.128 | 1.226 | 1.149 | $256 \times 256$ |
| 1000 | 0.234 | 1.527 | 0.061 | 1.465 | 1.500 | $128 \times 128$ |
| 1000 | 0.234 | 1.417 | 0.076 | 1.341 | 1.407 | $256 \times 256$ |

Table 2
3-D grid details

| Grid | Spanwise extension | Grid sizes | Total number of volumes | Volume sizes on cylinder surface |
|---|---|---|---|---|
| D | $\pi/2D$ | $128 \times 128 \times 32$ | 524,288 | |
| E | $\pi D$ | $128 \times 128 \times 64$ | 1,048,576 | $0.0245D \times 0.0245D$ |
| F | $2\pi D$ | $128 \times 128 \times 128$ | 2,097,152 | |

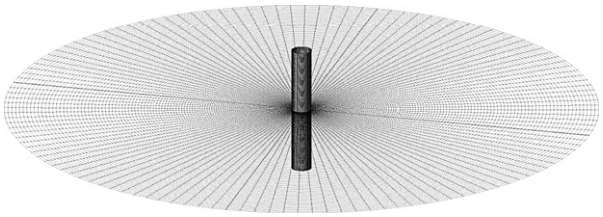

Fig. 2. Grid F—$128 \times 128 \times 128$.

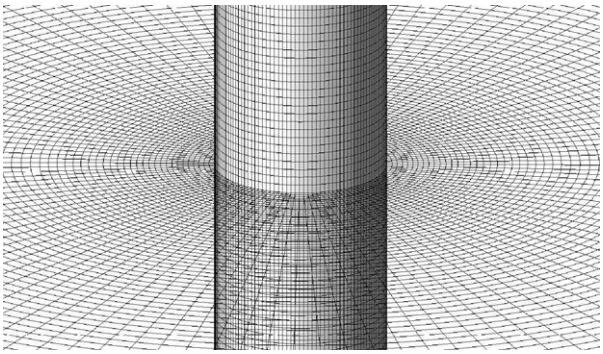

Fig. 3. Grid details near the cylinder.

Table 3
3-D flow past a circular cylinder—case details

| Re | Re step | Time step | Minimum residue | | Turbulence model | Simulation time |
|---|---|---|---|---|---|---|
| | | | Paper equations | Poisson | | |
| 40 | – | 0.0100 | | | | |
| 125–375 | 25 | 0.0100 | $10^{-7}$ | $10^{-5}$ | LES-SF | 300 |
| 400–1000 | 100 | 0.0050 | | | | |

To assess the difference between the 2-D and 3-D results, the same cases as for the 2-D flows were tested on each of the three grids D, E and F, using the Structure Function LES turbulence model. The general details of the cases set-up are given in Table 3.

### 3.2. Three-dimensional lift, drag and Strouhal number

One of the key results in the analysis of the flow past a circular cylinder is the overall force acting on the cylinder. Generally, this force is decomposed into a streamwise component, i.e., the drag force, and a transverse component,

i.e., the lift force. Both the drag and lift coefficients are calculated over the duration of the simulation and their behaviour over time can be analyzed to reveal characteristic aspects of the flow past a circular cylinder. Among other factors, the Strouhal number can be determined using the lift force coefficient history.

In the present section, the history of the force coefficients for the three grids D, E and F is presented and analysed over the range of Reynolds numbers considered. Key relationships between the lift, drag, Strouhal number and Reynolds number are then deduced and discussed.

As the simulations are carried out using a boundary-condition-driven method, the local Reynolds number around the cylinder is progressively increased. As a consequence, the flow will always be 2-D in the initial stages of the simulations. Whether three-dimensionalities appear in the flow after a certain time is then dependent upon the considered Reynolds number. It is thus expected that the history of the force coefficients will reflect such a transition from 2-D to 3-D flows for Reynolds numbers above approximately 200.

Tables 4, 5 and 6 display the results obtained for grids D, E and F. The history of the force coefficients for the three grids as illustrated in Fig. 4 for $\mathrm{Re} = 700$ reveals several interesting features.

The first noticeable one is the transition between the purely 2-D flow and the 3-D flow mentioned above. The regular sinusoidal oscillations with constant amplitudes of both the lift and drag coefficients for $\mathrm{Re} \geqslant 300$ change to oscillations with more irregular amplitudes when the 3-D instabilities appear. These changes in the force coefficient traces have some consequences on the Strouhal number obtained. For the 2-D part of the flow, the frequency of oscillations of the lift coefficient, i.e., the frequency of the vortex shedding should match the one found in the 2-D simulations, while the frequency of the oscillation after the wake becomes 3-D should be different. In the power spectrum of the lift coefficient (Fig. 4), a secondary weaker peak appears and separates from the main one as Re is increased. Although it is sometimes difficult to see it clearly, this secondary peak occurs in fact at the Strouhal frequency of the 2-D part of the flow.

As the spanwise extension is increased from $\pi/2$ for grid D to $2\pi$ for grid F, the occurrence of the oscillation of the coefficients is delayed in time. Furthermore, the period over which the flow is 2-D increases with the spanwise extension. This difference is particularly noticeable when comparing the traces obtained with grid D with the traces from the other two grids. Interestingly, one could have supposed that the opposite should occur as the shorter spanwise extension would promote 2-D flows.

Another interesting feature that appears for $\mathrm{Re} \geqslant 300$ is the quasiperiodic beat phenomenon. As can be observed in Fig. 4, the beat is more pronounced as the spanwise extension is decreased. This seems to contradict the findings of Lei et al. (2001) who could only observe the quasiperiodic beat phenomenon for extensions greater than two cylinder diameters at $\mathrm{Re} = 1000$. An explanation may be because of the coarser grids used in their simulation. Early tests carried out on coarse grids in the present research revealed much more regular behaviour of the force coefficients than for finer

Table 4
Force coefficients for grid D

| Re | St | $\overline{C_D}$ | $\overline{C_{D_v}}$ | $\overline{C_{D_p}}$ | $\widehat{C_L}$ | $\widehat{C_{L_v}}$ | $\widehat{C_{L_p}}$ |
|---|---|---|---|---|---|---|---|
| 100 | 0.166 | 1.328 | 0.309 | 1.019 | 0.328 | 0.038 | 0.296 |
| 125 | 0.181 | 1.314 | 0.273 | 1.041 | 0.428 | 0.043 | 0.392 |
| 150 | 0.181 | 1.310 | 0.246 | 1.064 | 0.521 | 0.047 | 0.482 |
| 175 | 0.190 | 1.313 | 0.225 | 1.088 | 0.606 | 0.049 | 0.565 |
| 200 | 0.195 | 1.318 | 0.207 | 1.111 | 0.683 | 0.050 | 0.642 |
| 225 | 0.200 | 1.324 | 0.193 | 1.131 | 0.752 | 0.051 | 0.710 |
| 250 | 0.200 | 1.318 | 0.179 | 1.140 | 0.812 | 0.051 | 0.771 |
| 275 | 0.205 | 1.308 | 0.166 | 1.142 | 0.842 | 0.049 | 0.801 |
| 300 | 0.200 | 1.307 | 0.156 | 1.151 | 0.784 | 0.044 | 0.749 |
| 325 | 0.205 | 1.314 | 0.147 | 1.166 | 0.840 | 0.044 | 0.804 |
| 350 | 0.205 | 1.317 | 0.139 | 1.177 | 0.880 | 0.044 | 0.845 |
| 375 | 0.210 | 1.303 | 0.131 | 1.172 | 0.868 | 0.041 | 0.836 |
| 400 | 0.205 | 1.306 | 0.125 | 1.181 | 0.922 | 0.041 | 0.890 |
| 500 | 0.215 | 1.262 | 0.102 | 1.160 | 1.055 | 0.039 | 1.023 |
| 600 | 0.205 | 1.277 | 0.087 | 1.190 | 1.120 | 0.036 | 1.091 |
| 700 | 0.205 | 1.242 | 0.075 | 1.167 | 1.126 | 0.032 | 1.101 |
| 800 | 0.215 | 1.178 | 0.064 | 1.115 | 0.852 | 0.025 | 0.834 |
| 900 | 0.205 | 1.229 | 0.059 | 1.171 | 1.026 | 0.024 | 1.006 |
| 1000 | 0.215 | 1.155 | 0.051 | 1.104 | 0.651 | 0.015 | 0.638 |

Table 5
Force coefficients for grid E

| Re | St | $\overline{C_D}$ | $\overline{C_{D_v}}$ | $\overline{C_{D_p}}$ | $\widehat{C_L}$ | $\widehat{C_{L_v}}$ | $\widehat{C_{L_p}}$ |
|---|---|---|---|---|---|---|---|
| 100 | 0.166 | 1.331 | 0.314 | 1.018 | 0.331 | 0.039 | 0.299 |
| 125 | 0.176 | 1.318 | 0.279 | 1.039 | 0.433 | 0.044 | 0.396 |
| 150 | 0.181 | 1.315 | 0.253 | 1.062 | 0.528 | 0.048 | 0.488 |
| 175 | 0.190 | 1.318 | 0.232 | 1.086 | 0.616 | 0.051 | 0.574 |
| 200 | 0.200 | 1.323 | 0.215 | 1.108 | 0.696 | 0.052 | 0.653 |
| 225 | 0.200 | 1.328 | 0.201 | 1.127 | 0.767 | 0.053 | 0.724 |
| 250 | 0.205 | 1.328 | 0.188 | 1.140 | 0.830 | 0.054 | 0.787 |
| 275 | 0.205 | 1.309 | 0.175 | 1.134 | 0.885 | 0.054 | 0.842 |
| 300 | 0.205 | 1.302 | 0.155 | 1.146 | 0.850 | 0.047 | 0.810 |
| 325 | 0.205 | 1.302 | 0.146 | 1.156 | 0.839 | 0.044 | 0.803 |
| 350 | 0.205 | 1.292 | 0.138 | 1.154 | 0.819 | 0.041 | 0.786 |
| 375 | 0.205 | 1.264 | 0.128 | 1.136 | 0.845 | 0.040 | 0.813 |
| 400 | 0.205 | 1.264 | 0.122 | 1.142 | 0.795 | 0.036 | 0.766 |
| 500 | 0.205 | 1.256 | 0.101 | 1.154 | 0.830 | 0.032 | 0.804 |
| 600 | 0.215 | 1.211 | 0.084 | 1.126 | 0.781 | 0.027 | 0.759 |
| 700 | 0.205 | 1.213 | 0.074 | 1.140 | 0.851 | 0.026 | 0.830 |
| 800 | 0.205 | 1.177 | 0.064 | 1.113 | 0.890 | 0.024 | 0.872 |
| 900 | 0.219 | 1.195 | 0.058 | 1.138 | 0.826 | 0.020 | 0.808 |
| 1000 | 0.215 | 1.203 | 0.052 | 1.151 | 0.717 | 0.017 | 0.703 |

Table 6
Force coefficients for grid F

| Re | St | $\overline{C_D}$ | $\overline{C_{D_v}}$ | $\overline{C_{D_p}}$ | $\widehat{C_L}$ | $\widehat{C_{L_v}}$ | $\widehat{C_{L_p}}$ |
|---|---|---|---|---|---|---|---|
| 100 | 0.161 | 1.327 | 0.309 | 1.019 | 0.328 | 0.038 | 0.296 |
| 125 | 0.176 | 1.313 | 0.273 | 1.040 | 0.428 | 0.043 | 0.392 |
| 150 | 0.186 | 1.310 | 0.246 | 1.064 | 0.521 | 0.047 | 0.482 |
| 175 | 0.190 | 1.313 | 0.225 | 1.088 | 0.606 | 0.049 | 0.565 |
| 200 | 0.195 | 1.318 | 0.207 | 1.111 | 0.683 | 0.050 | 0.642 |
| 250 | 0.205 | 1.307 | 0.177 | 1.130 | 0.811 | 0.051 | 0.769 |
| 275 | 0.200 | 1.268 | 0.162 | 1.106 | 0.846 | 0.050 | 0.805 |
| 300 | 0.205 | 1.287 | 0.154 | 1.132 | 0.745 | 0.042 | 0.709 |
| 325 | 0.205 | 1.299 | 0.146 | 1.153 | 0.810 | 0.042 | 0.776 |
| 375 | 0.205 | 1.268 | 0.129 | 1.139 | 0.782 | 0.037 | 0.752 |
| 400 | 0.205 | 1.262 | 0.122 | 1.140 | 0.777 | 0.036 | 0.748 |
| 500 | 0.205 | 1.253 | 0.101 | 1.151 | 0.820 | 0.032 | 0.793 |
| 700 | 0.205 | 1.224 | 0.074 | 1.150 | 0.783 | 0.024 | 0.765 |
| 800 | 0.205 | 1.193 | 0.064 | 1.129 | 0.732 | 0.020 | 0.716 |
| 900 | 0.205 | 1.237 | 0.059 | 1.178 | 0.703 | 0.018 | 0.690 |
| 1000 | 0.215 | 1.200 | 0.052 | 1.148 | 0.687 | 0.016 | 0.674 |

grids at $\mathrm{Re} \approx 1000$. It seems thus reasonable to suggest that a coarse grid that cannot capture the small-scale instabilities, and would not be able to predict accurately the forces acting on the cylinder.

The secondary oscillations (quasi-periodic beat) observed in the lift coefficient traces are such that in the case of the lower $\pi D/2$ spanwise extension, the lift reaches both lower and higher values than for the greater extensions. This is particularly evident for Reynolds numbers between 350 and 700. As a consequence, the maximum lift values obtained with grid D are expected to be higher than for the other two grids for this range of Re. For the lower and higher Reynolds numbers, the beat is not so accentuated and matches that observed in the traces obtained with grid E and F in a better fashion.

Some of the findings described above are essential to understand the relationships between the Reynolds number and the Strouhal number, the average drag coefficient and maximum lift coefficient. In Fig. 5, a comparison is made between the Strouhal–Reynolds number relationship for the three grids studied and the data obtained experimentally

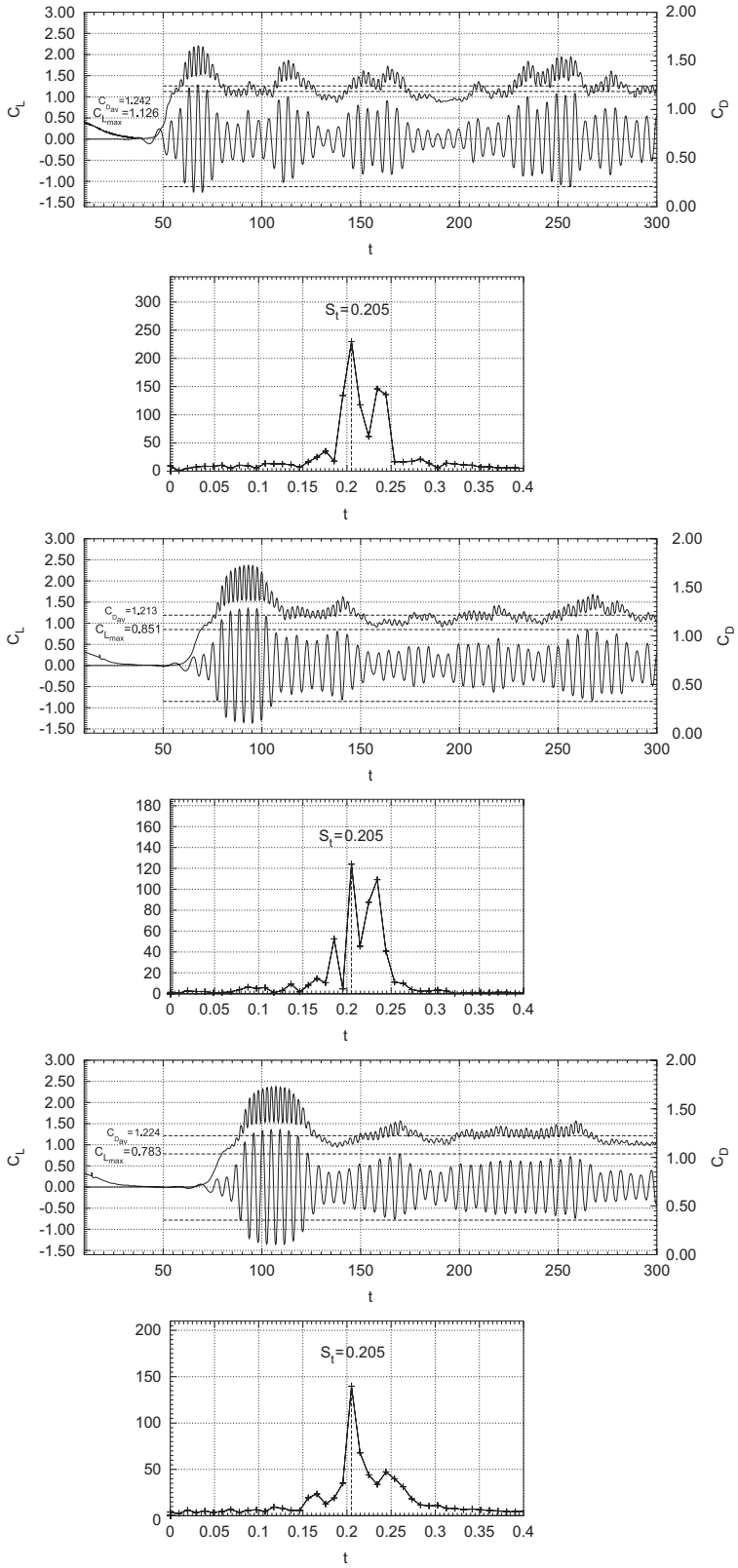


Fig. 4. Force coefficients history (left) and power spectrum (right) at Re = 700 for grids D (upper), E (middle) and F (lower).

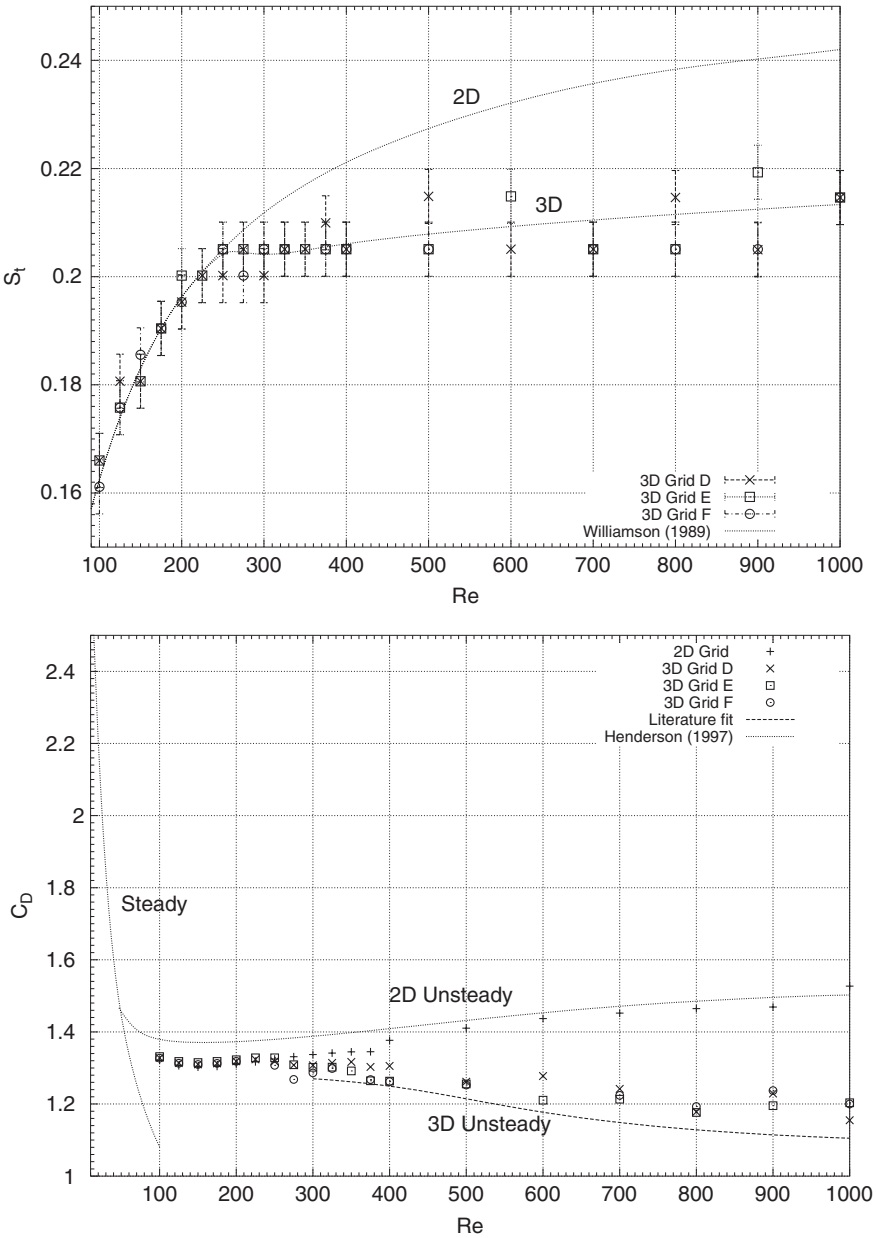


Fig. 5. Relationship between St and Re (top) and between $C_{D_{\mathrm{av}}}$ and Re (bottom).

by Williamson (1996). The results show very good agreement with the experimental data. In particular, the transition between the 2-D and 3-D parts of the curves is well predicted on all three grids.

The drag coefficient versus Reynolds number relationship shown in Fig. 5 also exhibits a very good correspondence with the data found in the literature. For the higher Reynolds numbers, there exists a relative scatter in the results. This could be due to a resolution issue in the FFT method where the frequency obtained depends highly on the time over which the sampling is taken and the number of periods occurring over that time. The error bars on the figure are an indication of the frequency resolution and, thus, the error on the calculated Strouhal number. However, for each Reynolds number investigated, the Strouhal numbers obtained with the present method fall in the ranges found in the literature.

It thus seems difficult to assess the difference between the three grids from the St versus Re and $C_{D_{\mathrm{av}}}$ versus Re relationships alone. Fig. 5 contains the numerical results of Henderson (1997) and shows a range of data from both

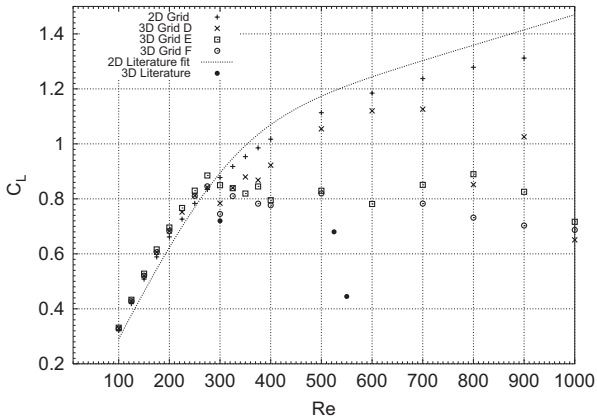


Fig. 6. Relationship between $C_{L_{\max}}$ and Re.

experiments and computational methods. Henderson's (1997) numerical results indicate a value of $C_D = 1.1$ for $\mathrm{Re} = 1000$, which interestingly is very similar to that calculated and given in Table 5. There are no reasons given in Henderson (1997) for the differences between experimental and computational values for the 3-D case at high Reynolds numbers. The computational method described in earlier sections of our paper certainly produced a solution that converged; however, a different mesh distribution in the cylinder wake could produce values of $C_D$ that are closer to the experimental data. However, it must be borne in mind that each experimental data point has associated error bars and it is notoriously difficult to gain consistent experimental results, and subtle changes in the drag curve are lost in the associated experimental scatter.

The differences between the results obtained at different spanwise extensions starts showing when looking at the relationship between $C_{L_{\max}}$ and Re as illustrated in Fig. 6. Although for Reynolds numbers up to $\approx 350$ similar results are found for the three grids, the maximum lift coefficients found for grid D for $350 \leqslant \mathrm{Re} \leqslant 700$ are overpredicted and thus a lot closer to the 2-D results than the other two grids. This is a consequence of the more accentuated quasi-beating phenomenon observed in the coefficient traces and discussed previously. For $\mathrm{Re} \geqslant 700$, the lift coefficients obtained with grid D tend toward those obtained with the other two grids suggesting that the three curves would eventually converge for $\mathrm{Re} \geqslant 1000$.

Despite the differences in results discussed above, the analysis of the force coefficients is not sufficient to clearly assess the influence of the spanwise extension on the 3-D wake behind a circular cylinder. In particular, the quasi-beating phenomenon observed for all three grids suggests that differences in the wake of the cylinder could be observed for the various spanwise extensions. It is thus necessary to investigate the vortex shedding using adequate visualization.

### 3.3. Vortex shedding modes

In the present section, an analysis of a visualization of the results obtained is carried out. The core part of the analysis will focus on the components of vorticity in the wake of the cylinder. The visualization was developed using the IBM Data Explorer software (see http://www.opendx.org).

It has been shown (Williamson, 1988) that there exist two modes of vortex shedding in the transition to 3-D wake. Furthermore, each of these two modes corresponds to a spanwise instability in the wake and has a distinct geometry (Williamson, 1996). In mode A, the streamwise vortices of one sign are in a staggered arrangement from one braid region to the next, while in mode B, an in-line arrangement of streamwise vortices of the same sign can be seen.

In addition to their specific geometry, modes A and B exhibit very different spanwise wavelengths. Although a relative scatter of the data can be seen in the literature, it is usually found that, in mode A, the spanwise wavelength is of about $4D$, while it is of about $1D$ for mode B. As a consequence, grid F used in the present research should be adequate to capture mode A as its spanwise extension is $2\pi D$. Grid E of spanwise extension $\pi D$ might be a bit too short to capture fully the mode, and grid D with an extension of $\pi D/2$ should not allow for mode A to be well predicted. All three grids on the other hand should be able to capture the vortex shedding mode B.

#### 3.3.1. Mode A

In Fig. 7, the influence of the spanwise extension is shown by comparing the streamwise and spanwise components of vorticity at $\mathrm{Re} = 200$ on the three grids D, E and F. Grid F clearly captures mode A and exhibits a spanwise wavelength

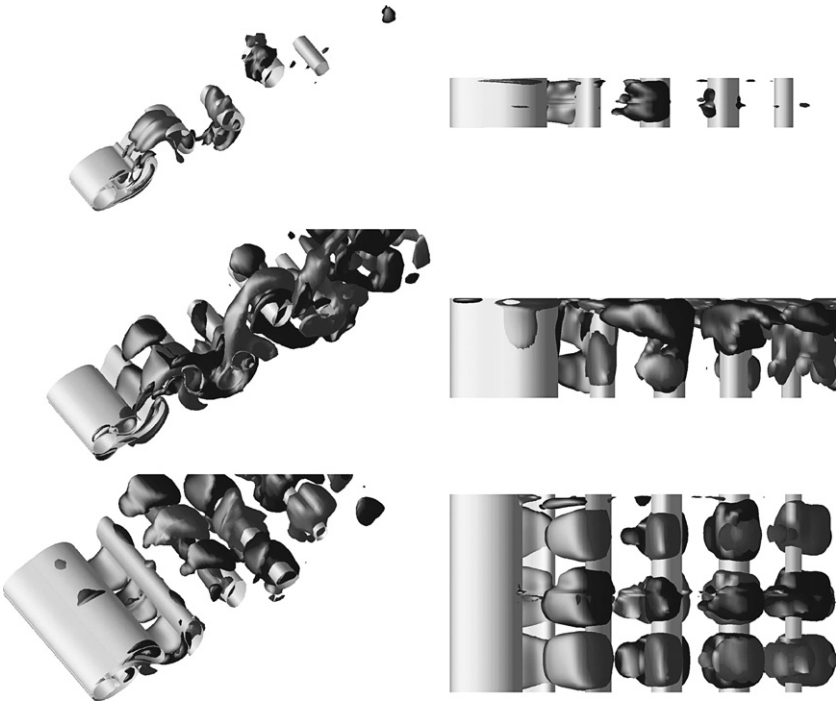

Fig. 7. Domain spanwise extension influence on mode A vortex shedding. Comparison of the streamwise and spanwise components of vorticity for grid D (top), grid E (middle) and grid F (bottom) at Re = 200.

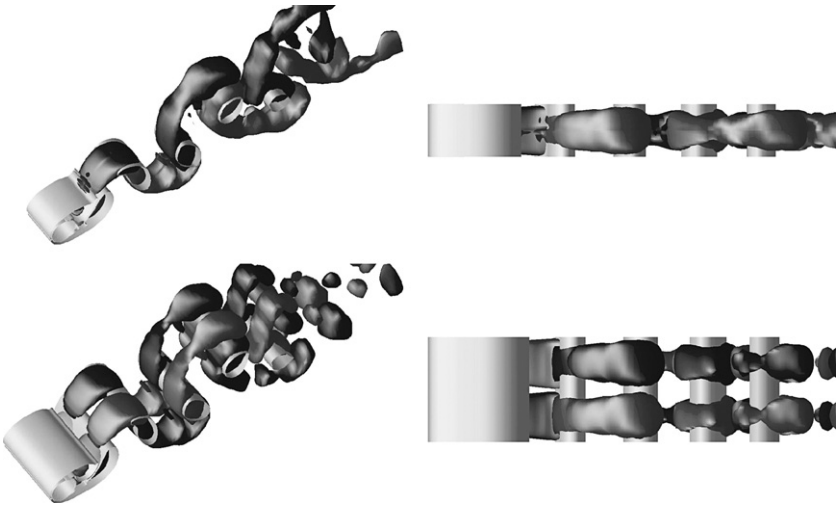

Fig. 8. Mode A vortex shedding: comparison of the streamwise and spanwise components of vorticity for grids D and E at Re = 225.

of about $4D$. Since this is slightly more than the spanwise extension of grid E, it is understandable that the visualization shows a partially predicted mode A on grid E. Another interesting comment can be made from this visualization regarding grid D. Although the spanwise extension of grid D is far too short to capture mode A, its extension is close to half a wavelength, thus explaining the reason for seeing what appears to be half of the spanwise period.

It thus appears that grid D, through the nonperiodic spanwise boundary conditions, is capable of capturing half of the spanwise wavelength of the vortex shedding. In Fig. 8, the visualization of the streamwise and spanwise vorticity for grid D and E at Re = 225 supports this argument by showing a complete wavelength period in the case of grid E and an exact half period for grid D. Although it was not possible to produce a comparative visualization for grid F owing to

the absence of results at this particular Reynolds number, it appears that for Re = 225, the spanwise wavelength is closer to $\pi D$, thus suggesting that the vortex shedding mode A may have indeed different spanwise wavelengths depending on the Reynolds number. This could explain the relative scatter of data reported by Williamson (1996).

The comparison between the experimental visualization of mode A by Williamson (1996) and the present numerical simulation at Re = 200 shown in Fig. 9 shows a remarkably similar pattern in the vorticity. Furthermore, the wavelength shown in both cases is in very good agreement. This confirms that the present method is capable of accurately predicting the vortex shedding mode A, provided the grid possesses sufficient spanwise extension. Although grid E resulted in a good prediction of the wake for Re = 225 and grid D could predict half a wavelength, most of mode A occurs at a spanwise extension of about $4D$. It can be concluded that a spanwise extension of at least $2D$ is required to capture half a wavelength at mode A and one of at least $4D$ for the complete wavelength.

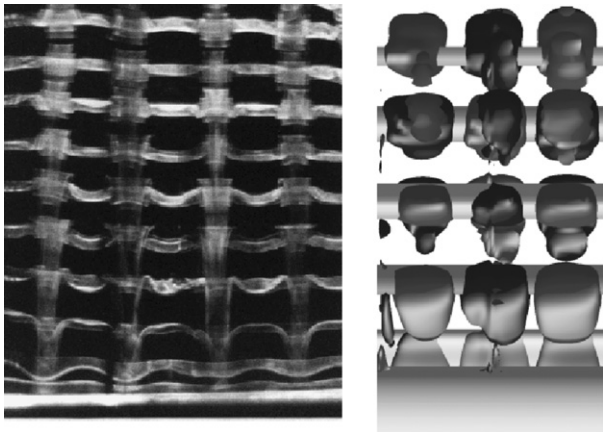

Fig. 9. Mode A vortex shedding at Re = 200. Left: experiment (Williamson, 1996); right: present simulation.

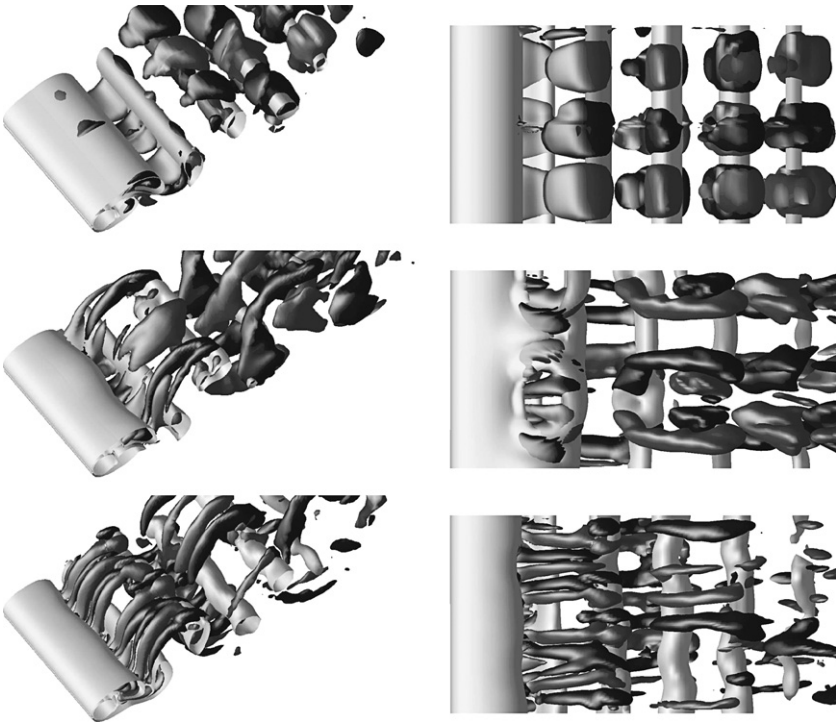

Fig. 10. Mode A to mode B transition. Streamwise and spanwise components of vorticity for grid F, mode A at Re = 200 (top), transition at Re = 250 (middle), and mode B at Re = 300 (bottom).

#### 3.3.2. Mode B

The transition to the vortex shedding mode B is somewhat difficult to investigate as numerous simulations would be required in the Reynolds number range where it occurs. Since at $\mathrm{Re} = 200$ it is clearly established that mode A is occurring, and since the transition occurs approximately between $\mathrm{Re} = 230$ and 260, a visualization of the vorticity in the wake of the cylinder for $200 \leqslant \mathrm{Re} \leqslant 300$ should give an insight into the transition phase.

A confirmation of this hypothesis is given in Fig. 10 where clear evidence of the occurrence of both modes A and B are provided for $\mathrm{Re} = 200$ and 300 on grid F. The visualization at $\mathrm{Re} = 250$ shown in this figure is extremely interesting as it exhibits a vortex pattern complying with mode A but with much thinner vortex layers, indicating the transition to mode B. Furthermore, a clear difference with the pure mode A vortex shedding patterns can be seen in the spanwise component of vorticity.

Further evidence of the transition between the two vortex shedding modes is given in Fig. 11 where the transversal component of velocity is shown in the symmetry plane in the wake of the cylinder. A clear wavy pattern shows at $\mathrm{Re} = 250$ but does not appear at $\mathrm{Re} = 200$. At $\mathrm{Re} = 300$, although there seems to be an oscillation in the spanwise direction of the transversal component of velocity, the patterns exhibited are much more uniform than for $\mathrm{Re} = 250$.

For $\mathrm{Re} \geqslant 300$, the shedding of vortices in the wake of the cylinder follows the pattern of mode B. As shown in Fig. 12, the prediction of mode B with grid F compares remarkably well with both experimental (Williamson, 1996) and numerical (Poncet, 2001) results found in the literature.

Since the wavelength of mode B is close to $1D$, the three spanwise extensions are sufficient to capture the mode as illustrated by Fig. 13. Indeed, the visualization of the wake vorticity for the three grids reveals that for $\mathrm{Re} \geqslant 300$, the spanwise wavelength is approximately equal to $1D$ at $\mathrm{Re} = 300$, decreasing slightly as the Reynolds number increases to approximately $0.8D$ for $\mathrm{Re} = 1000$.

#### 3.3.3. Spanwise wavelength and extension

Determining the wavelength is rather difficult from the visualization, particularly at the higher Reynolds number where the wake is more chaotic. However, by looking at the wake close to the cylinder, i.e., at approximately $x/D = 3$, it is possible to estimate the wavelength of the 3-D instabilities by averaging a number of periods over the spanwise extension of the cylinder.

Although using such a method may appear rather inaccurate, considering that very few periods can be observed particularly for the shortest extension (grid D), the resulting estimation agrees rather well with Williamson's (1996) measurements as shown in Fig. 14. The separation between the wavelengths at mode A and those at mode B clearly appears and compares well with Williamson's trends.

Furthermore, the wavelengths obtained for grids E and F are similar, those obtained for grid D at a spanwise extension of $\pi D/2$ are slightly shorter for the Reynolds numbers between 250 and 600. Considering that only a single period could be measured from the visualization of the spanwise vorticity on grid D, the estimation could be rather inaccurate for this particular grid. However, the fact that the wavelength is systematically lower suggests that the spanwise extension and most probably the boundary conditions imposed in that direction affected the 3-D instabilities.

### 3.4. Summary

The investigation of the effects of the spanwise extension on the 3-D wake of a circular cylinder revealed several interesting facts.

The analysis of the force coefficients obtained for the three spanwise extensions led to the conclusion that the $\pi D$ (grid E) and $2\pi D$ (grid F) extensions produced similar results. In the case where the extension was only of $\pi D/2$, both Strouhal number and average drag coefficient were reasonably predicted. However, owing to the more pronounced quasiperiodic beat phenomenon, the lift coefficient amplitude was overpredicted. Nevertheless, the trend observed in the lift coefficient amplitude for that extension suggested that as the Reynolds number is increased, the prediction of the force coefficient for grid D would converge with the other two grids.

The visualization of the vorticity in the wake of the cylinder confirmed that both grids D and E are not well suited to predict the vortex shedding mode A across the whole range of Reynolds number where it occurs. However, a very interesting result at $\mathrm{Re} = 225$ showed that grid D was capable of predicting an exact half wavelength of mode A. Grid F on the other hand allowed for mode A to be fully captured and the transition between modes A and B to be visualized.

For the vortex shedding mode B, it was found that all three extensions and in particular the shortest $\pi/2$ extension produced similar wake vorticity patterns. The agreement between the spanwise and streamwise vorticity observed for

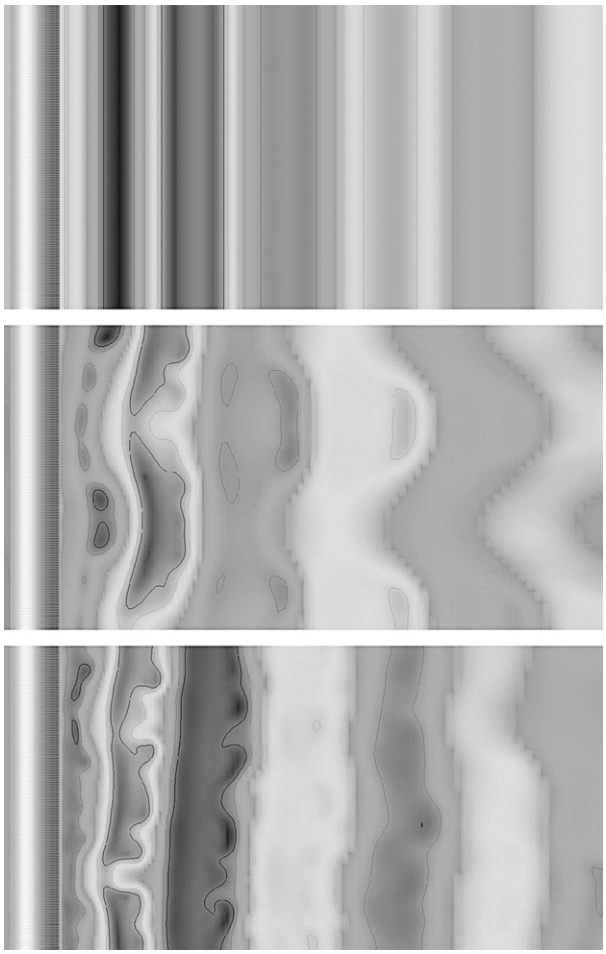

Fig. 11. Mode A to mode B transition. Transversal components of velocity ($V$) for grid F. Mode A at Re = 200 (top), transition at Re = 250 (middle), and mode B at Re = 300 (bottom).

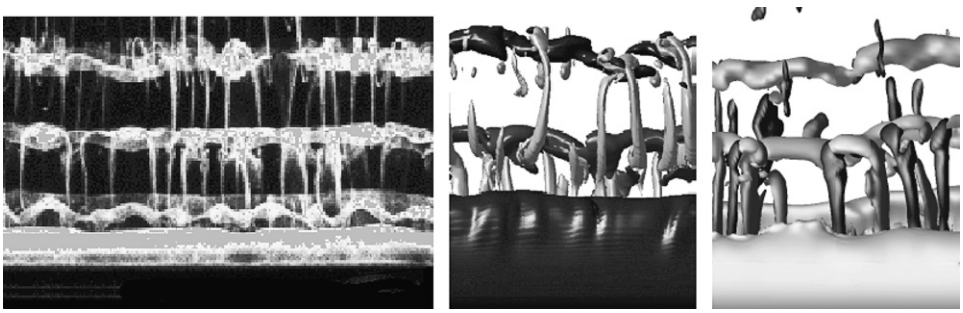

Fig. 12. Vortex shedding in the wake of a circular cylinder at Re = 400. From left to right: experimental (Williamson, 1996) numerical (Poncet, 2001), and present numerical solution.

the three grids therefore suggests that the extension of grid D is sufficient to predict the flow past a circular cylinder at Reynolds numbers in the mode B range.

Finally, the estimated spanwise wavelength obtained from the visualization of the 3-D instabilities compared very well with experimental data found in the literature for all three spanwise extensions investigated thus confirming that the 3-D instabilities are well predicted in all three cases.

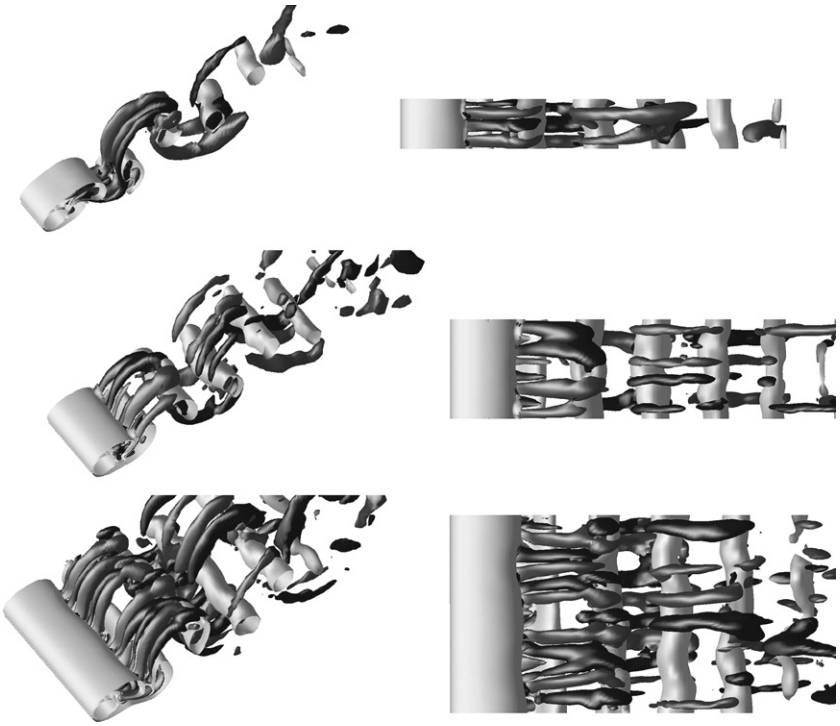

Fig. 13. Mode B vortex shedding: comparison of the streamwise and spanwise components of vorticity for grid D (top), grid E (middle) and grid F (bottom) at Re = 300.

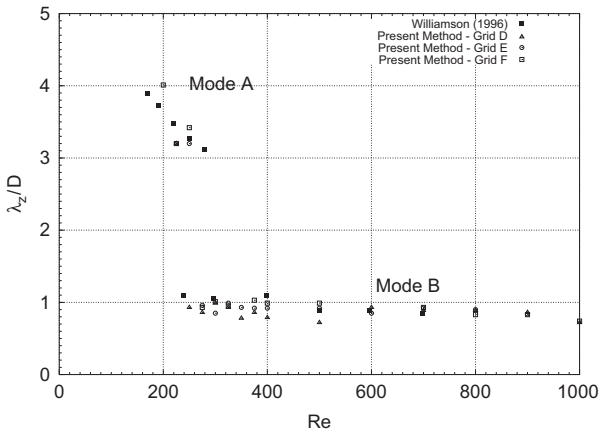


Fig. 14. Spanwise wavelengths of the 3-D instabilities.

## 4. Conclusions

In light of these findings, it is possible to conclude that a finite spanwise extension of the cylinder is sufficient to predict the flows past an infinitely long circular cylinder in the considered range of Reynolds numbers. Clear evidence was produced showing that the minimum spanwise extension required for flows at low Reynolds numbers up to about 300 was in the region of four cylinder diameters. For higher Reynolds numbers, a shorter spanwise extension between $\pi D/2$ and $\pi D$ is sufficient to predict accurately all the characteristic components of the flow, namely the force coefficients, the Strouhal number and also the 3-D instabilities and their wavelength. Furthermore, it is reasonable to suggest that such conclusions could extend beyond the range of Reynolds number studied in the present investigation.

**Acknowledgements**

The authors would like to thank the reviewers for their excellent suggestions for improvement of the substance of the paper. One of the authors (Labbé) would like to thank the School of Engineering Sciences of the University of Southampton for financing his doctoral studies.

## Appendix A

### A.1. Flow governing equations

The incompressible Navier–Stokes equations in curvilinear coordinates and filtered for the large eddy simulation turbulence model can be written as follows in a nondimensional form and using tensor notation:

*Continuity*:

$$\frac{\partial(J\overline{U^i})}{\partial\xi_i} = 0; \tag{A.1}$$

*Momentum*:

$$\frac{\partial}{\partial t}(J\bar{u}_i^*) + \frac{\partial}{\partial\xi_k}(\overline{U_r}^{*k}\bar{u}_i^*) = -J^{-1}S_i^j\frac{\partial\bar{q}}{\partial\xi_j} + \frac{\partial}{\partial\xi_k}\left[\left(\frac{1}{\mathrm{Re}} + \frac{1}{\mathrm{Re}_t}\right)\left(J^{-1}S_j^kS_j^l\frac{\partial\bar{u}_i^*}{\partial\xi_l}\right)\right]; \tag{A.2}$$

where $J$ is the Jacobian of the coordinate transformation,

$$J = \frac{D(x,y,z)}{D(\xi,\eta,\zeta)}, \tag{A.3}$$

$S_j^i$ are the metrics of the transformation defined by,

$$S_j^i = J\frac{\partial\xi_i}{\partial x_j}, \quad \text{with } i,\ j \text{ and } k \text{ cyclic}, \tag{A.4}$$

$\overline{U}^j$ is the filtered contravariant component of velocity,

$$\overline{U}^j = S_i^j\bar{u}_i, \tag{A.5}$$

$\overline{U_r}^j$ is the filtered contravariant component of relative velocity,

$$\overline{U_r}^j = S_i^j(\bar{u}_i - \overline{u_g}_i), \tag{A.6}$$

with $\overline{u_g}_i$ being the filtered grid velocity component, and $\bar{q}$ the pseudo-pressure defined by,

$$\bar{q} = \bar{p} - \tfrac{1}{3}\tau_{ll}. \tag{A.7}$$

In Eq. (A.2), $\mathrm{Re}_t$ is the turbulent Reynolds number as obtained using one of the Structure Function LES models (Métais and Lesieur, 1992):

$$\mathrm{Re}_t = \frac{U_\infty D}{0.063\Delta\sqrt{\overline{F}_2(\xi,\Delta t)}}, \tag{A.8}$$

where $\Delta$ is the filter width, usually taken as an average of the mesh sizes, and where the function $\overline{F}_2$ can be obtained from

$$\Delta = \sqrt[3]{\Delta x\Delta y\Delta z}, \quad \overline{F}_2 = \langle\|\mathbf{u}(\xi+\mathbf{r}) - \mathbf{u}(\xi)\|^2\rangle_{\|\mathbf{r}\|=1}. \tag{A.9}$$

### A.2. Boundary conditions implementation

From the discretization presented previously, and taking into account that the flow is solved using the primitive variables at the cell centre, it appears quite clear that the computational cell (Fig. A.1) used in solving the set of equations is composed of a single layer of cells around the current cell. However, at the domain boundaries, some of the neighbouring cells are nonexistent. To account for such absence of cells, a layer of so-called *ghost cells* is introduced around the block. Such ghost cells must then be set to represent appropriately the boundary conditions. Conveniently,

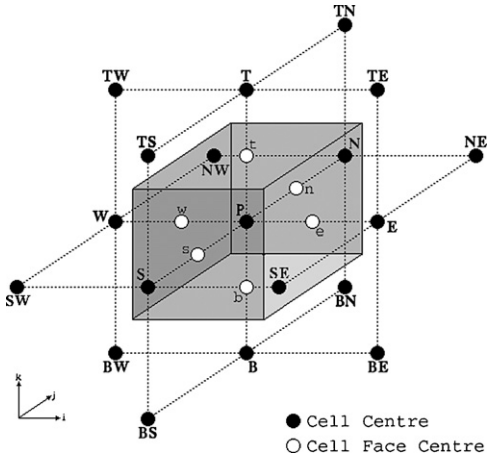


Fig. A.1. The computational cell.

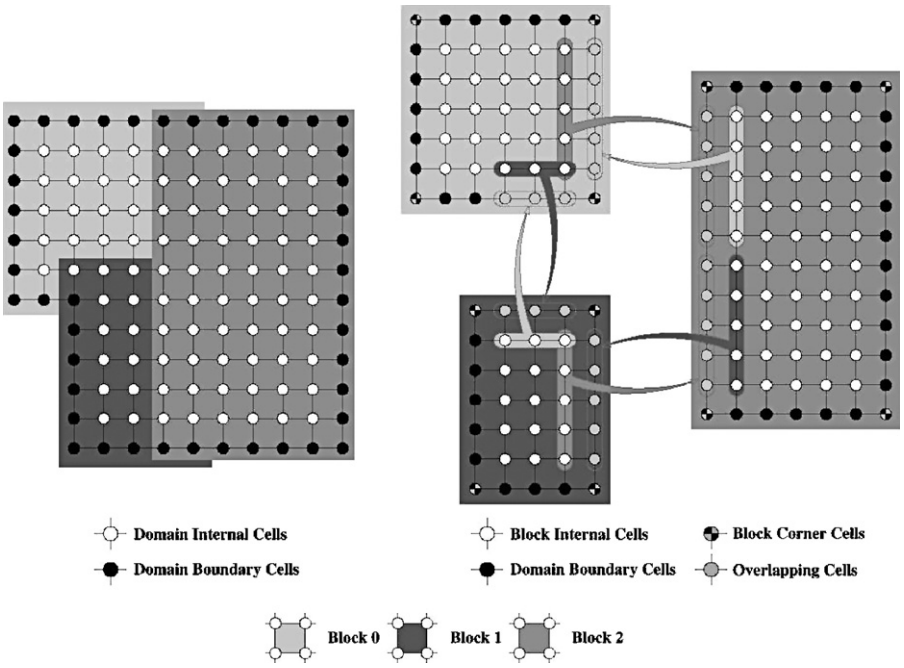


Fig. A.2. Multi-block domain decomposition.

these ghost cells can also be used to store information from adjacent blocks. The overlapping mesh strategy can thus be enforced in a straightforward manner using the ghost cells as the overlapping mesh area. Figure A.2 illustrates the subdivision of a domain into subdomains, and the data dependency between the subdomains with the overlapping mesh strategy.

In most cases, the boundary conditions used in the resolution of the Navier–Stokes equations are associated with the velocity, the nature of the problem usually not providing enough information on the pressure at the boundary except in cases such as free-surface flows. For each variable, i.e., velocity and pressure, the boundary $\Gamma$ is subdivided into $\Gamma_D$, where Dirichlet boundary conditions apply (such as $u = g(\vec{x}, t)$), and $\Gamma_N$, where Neumann boundary conditions apply (such as $\partial\phi/\partial n = 0$ where $n$ denotes the direction normal to the face of the cell where the condition applies).

In practical terms, the most common boundary conditions encountered in flow computations are the in-flow (constant or variable), the out-flow, the solid wall (fixed or moving), the symmetry and the periodic boundary conditions. Such conditions are enforced by setting the velocity and pressure in the ghost cells. Whether a Dirichlet or a

Neumann condition is to be used, all the boundary conditions (with the exception of the periodic one) can be interpreted in a generic formulation,

$$\phi_{GC} = C_1 + C_2\phi_{DC}, \tag{A.10}$$

where subscripts GC and DC denote the ghost cell and the neighbouring domain cell variables, respectively, $\phi$ can be the velocity components or the pressure and the constants $C_1$ and $C_2$ depend on the conditions to be applied. Table A.1 summarizes the constants used for each boundary condition.

One aspect of multi-block computation rarely described by other authors but however well known is that of block corners. In the particular case of 3-D computations, this extends to the block edges. The reason such corners and edges are of concern is related to the computational cell used in the discretization scheme and the boundary condition treatment. In the current implementation, this concerns the ghost cells variables to be set in the corners and edges of each block of the domain. At this point, it is important to note that only the edges of the blocks are of interest since the block corner values are never used in the computational stencil. In the 2-D case, the block corners are in fact a special case of block edges. Figure A.3 illustrates a block edge with the notation adopted for the variables to be set. The subscripts DCE and GCE denote variable in the domain edge (domain cell) and in the block edge (ghost cell).

It can be shown that all the possible combinations of boundary conditions can be enforced at the block edges using a generalized formulation where the value of the velocity in the edge ghost cell can be set by

$$\mathbf{u}_{GCE} = C_3\mathbf{u}_{GC0} + C_4\mathbf{u}_{GC1} + C_5\mathbf{u}_{DCE}, \tag{A.11}$$

where $C_3$, $C_4$ and $C_5$ are constants set according to the boundary conditions on each side of the edge. Table A.2 summarizes the constants used for each case.

For the pressure, a simple extrapolation technique is used based on the value of the pressure in the ghost cells on each side of the edge.

### A.3. Overall flow solution procedure

Having derived the various equations to be solved and suitable methods to solve them, the general procedure for the solution of the flow will be summarized in algorithm A.4. Since the solution is iterative, it is important to determine a stopping criterion for the loop. Generally, a maximum number of iteration (time steps) can be set, but in the case of a steady flow, the solution may converge before reaching the maximum number of iterations. A residue must thus be

Table A.1
Ghost cell boundary condition constants

| Boundary condition | Velocity | | Pressure | |
|---|---|---|---|---|
| | $C_1$ | $C_2$ | $C_1$ | $C_2$ |
| In-flow | $2\,\mathbf{u}_{inflow}$ | $-1$ | 0 | 1 |
| Out-flow | 0 | 1 | $2\,p_{ref}$ | $-1$ |
| Wall (fixed or moving) | $2\,\mathbf{u}_{wall}$ | $-1$ | 0 | 1 |
| | | Symmetry ($X_i$, $X_j$ plane) 1 for $u_i$ and $u_j$ | 0 | |
| | 0 | $-1$ for $u_k$ | 0 | 1 |

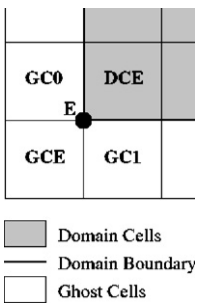


Fig. A.3. Block edges layout and notation.

Table A.2
Ghost cell boundary condition velocity constants at block edge

| Boundary condition | | | | | |
|---|---|---|---|---|---|
| Face0 | Face 1 | Edge type | $C_3$ | $C_4$ | $C_5$ |
| Solid | | | | | |
| Inflow | Outflow | 1 | 1 | 0 | 0 |
| Interface | | | | | |
| | Solid | | | | |
| Outflow | Interface | 0 | 0 | 1 | 0 |
| | Inflow | | | | |
| Inflow | Interface | | | | |
| Interface | Inflow | | | | |
| Solid | Solid | 0/1 | 0 | 0 | 1 |
| Inflow | Inflow | | | | |
| Outflow | Outflow | | | | |
| Solid | Interface | 1 | 1 | −1 | 1 |
| | Inflow | | | | |
| Interface | | | | | |
| Inflow | Solid | 0 | −1 | 1 | 1 |

calculated to assess the difference between the solutions at two consecutive time steps. If such a difference is below a certain tolerance level, the solution is assumed steady and thus converged. One way to determine the convergence is by comparing the velocity field between two consecutive time steps.

### A.4. Global flow solution algorithm

For $k = 1$ to $k = (\max.\ \text{num. of iteration})$:

(1) Solve the equations using SOR or CG.
(2) Solve the Poisson equation using SOR or CG.
(3) Solve the projection equations.
(4) Update the velocity and pressure in the ghost cells at boundaries, interface and block edges.
(5) Compute the local solution residue $R_{\text{local}}$ based on the velocity:

$$R_{\text{local}} = \frac{(\sum_i^n [\sum_{j=1}^3 |u_{j_i}^{(k+1)} - u_{j_i}^{(k)}|])}{(\sum_i^n [\sum_{j=1}^3 |u_{j_i}^{(k+1)}|])}.$$

(6) Determine the maximum residue across all the processes MPI: all reduce $R$.
(7) If $R <$(Min. Residue), then exit.

## References


Breuer, M., 1998. Numerical and modelling influences on large eddy simulations for the flow past a circular cylinder. International Journal of Heat and Fluid Flow 19, 512–521.

Breuer, M., 2000. A challenging test case for large eddy simulation: high Reynolds number circular cylinder flow. International Journal of Heat and Fluid Flow 21, 648–654.

Chorin, A., 1968. Numerical solution of the Navier–Stokes equations. Mathematical Computation 22, 745–762.

Cook, H., Beynet, P., Cornut, S., 2000. The challenge of VIV—an operator's view. In: WVIVOS—Workshop on Vortex-Induced Vibrations of Offshore Structures, vol. 1. São Paulo, Brazil.

Dalton, C., 2000. Calculation of flow past a circular cylinder using LES. In: WVIVOS—Workshop on Vortex-Induced Vibrations of Offshore Structures, vol. 1. São Paulo, Brazil.

Henderson, R.D., 1997. Nonlinear dynamics and pattern formation in turbulent wake transition. Journal of Fluid Mechanics 352, 65–112.

Kalro, V., Tezduyar, T., 1997. Parallel 3D computation of unsteady flows around circular cylinders. Parallel Computing 23, 1235–1248.

Labbé, D., 2004. A numerical investigation of the effects of the spanwise length on the three-dimensional wake of a circular cylinder. Ph.D. Thesis, University of Southampton, School of Engineering Sciences, Southampton, UK.

Lei, C., Cheng, L., Kavanagh, K., 2001. Spanwise length effects on three-dimensional modelling of flow over a circular cylinder. Computer Methods in Applied Mechanics and Engineering 910, 2909–2923.

Métais, O., Lesieur, M., 1992. Spectral large-lddy simulation of isotropic and stably stratified turbulence. Journal of Fluid Mechanics 239, 157–194.

Poncet, P., 2001. Méthodes particulaires pour la simulation des sillages tridimensionels. Ph.D. Thesis, Université de Grenoble 1—Joseph Fourier, Grenoble, France.

Roshko, A., 1955. On the wake and drag of bluff bodies. Journal of the Aeronautical Sciences 22, 124.

Thompson, M., Hourigan, K., Sheridan, J., 1996. Three-dimensional instabilities in the wake of a circular cylinder. Experimental Thermal and Fluid Science 12, 190–196.

Vandiver, J., 2000. Vortex-induced vibration of flexible risers in steady and unsteady flow. In: WVIVOS—Workshop on Vortex-Induced Vibrations of Offshore Structures, vol. 1. São Paulo, Brazil.

Williamson, C., 1988. The existence of two stages in the transition to three-dimensionality of a cylinder wake. Physics of Fluids 31, 3165–3168.

Williamson, C., 1996. Vortex dynamics in the cylinder wake. Annual Review of Fluid Mechanics 28, 477–539.

Wu, J., Sheridan, J., Welsh, M., Hourigan, K., 1996. Three-dimensional vortex structures in a cylinder wake. Journal of Fluid Mechanics 312, 201–222.

Zhang, J., Dalton, C., 1998. A three-dimensional simulation of a steady approach flow past a circular cylinder at low Reynolds number. International Journal for Numerical Methods in Fluids 26, 1003–1022.